

Article

Combining of MASW and GPR Imaging and Hydrogeological Surveys for the Groundwater Resource Evaluation in a Coastal Urban Area in Southern Spain

Francisco Javier Alcalá ^{1,2,*} , Pedro Martínez-Pagán ³ , Maria Catarina Paz ⁴ , Manuel Navarro ⁵,
Jaruselsky Pérez-Cuevas ⁶ and Francisco Domingo ⁷

¹ Instituto Geológico y Minero de España, 28003 Madrid, Spain

² Facultad de Ingeniería, Instituto de Ciencias Químicas Aplicadas, Universidad Autónoma de Chile, 7500138 Santiago, Chile

³ Department of Mining and Civil Engineering, Universidad Politécnica de Cartagena, 30203 Cartagena, Spain; p.martinez@upct.es

⁴ CIQuiBio, Polytechnic Institute of Setúbal, Barreiro School of Technology, 2839-001 Lavradio, Portugal; catarina.paz@estbarreiro.ips.pt

⁵ Department of Chemistry and Physics, Universidad de Almería, 04120 Almería, Spain; mnavarro@ual.es

⁶ Engineering Sciences, Pontificia Universidad Católica Madre y Maestra, 2748 Santo Domingo, Dominican Republic; jaruselskyperez@pucmm.edu.do

⁷ Estación Experimental de Zonas Áridas, Consejo Superior de Investigaciones Científicas, 04120 Almería, Spain; poveda@eeza.csic.es

* Correspondence: fj.alcala@igme.es; Tel.: +34-91-349-5840



Citation: Alcalá, F.J.;

Martínez-Pagán, P.; Paz, M.C.;

Navarro, M.; Pérez-Cuevas, J.;

Domingo, F. Combining of MASW and

GPR Imaging and Hydrogeological

Surveys for the Groundwater Resource

Evaluation in a Coastal Urban Area in

Southern Spain. *Appl. Sci.* **2021**, *11*,

3154. [https://doi.org/10.3390/](https://doi.org/10.3390/app11073154)

[app11073154](https://doi.org/10.3390/app11073154)

Academic Editors: Micòl Mastrocicco,

Francisco Javier Alcalá, Maria

Catarina Paz, Pedro Martínez-Pagán

and Fernando Monteiro Santos

Received: 27 February 2021

Accepted: 29 March 2021

Published: 1 April 2021

Publisher's Note: MDPI stays neutral with regard to jurisdictional claims in published maps and institutional affiliations.



Copyright: © 2021 by the authors.

Licensee MDPI, Basel, Switzerland.

This article is an open access article

distributed under the terms and

conditions of the Creative Commons

Attribution (CC BY) license ([https://creativecommons.org/licenses/by/](https://creativecommons.org/licenses/by/4.0/)

[https://creativecommons.org/licenses/by/](https://creativecommons.org/licenses/by/4.0/)

[4.0/](https://creativecommons.org/licenses/by/4.0/)).

Featured Application: Combining of geophysical and hydrogeological surveys provides basic insights for the shallow groundwater resource evaluation in a coastal urban area.

Abstract: This paper conceptualizes and evaluates the groundwater resource in a coastal urban area hydrologically influenced by peri-urban irrigation agriculture. Adra town in southern Spain was the case study chosen to evaluate the groundwater resource contributed from the northern steep urban sector (NSUS) to the southern flat urban sector (SFUS), which belongs to the Adra River Delta Groundwater Body (ARDGB). The methodology included (1) geological and hydrogeological data compilation; (2) thirteen Multichannel Analysis of Surface Waves (MASW), and eight Ground Penetrating Radar (GPR) profiles to define shallow geological structures and some hydrogeological features; (3) hydrogeological surveys for aquifer hydraulic definition; (4) conceptualization of the hydrogeological functioning; and (5) the NSUS groundwater resource evaluation. All findings were integrated to prepare a 1:5000 scale hydrogeological map and cross-sections. Ten hydrogeological formations were defined, four of them (Paleozoic weathered bedrock, Pleistocene littoral facies, Holocene colluvial, and anthropogenic filling) in the NSUS contributing to the SFUS. The NSUS groundwater discharge and recharge are, respectively, around 0.28 Mm³ year⁻¹ and 0.31 Mm³ year⁻¹, and the actual groundwater storage is around 0.47 Mm³. The groundwater renewability is high enough to guarantee a durable small exploitation for specific current and future urban water uses which can alleviate the pressure on the ARDGB.

Keywords: urban hydrogeology; hydrogeological map; multichannel analysis of surface waves; ground penetrating radar; aquifer geometry; groundwater resource evaluation; Adra town; Spain

1. Introduction

Water scarcity in many coastal drylands with limited surface water resources has propitiated high groundwater abstraction rates to supply the increasing urban, tourism, industrial, and agriculture demands [1]. This is the case in some coastal areas in Spain where aquifers play a critical role in sustaining the economy and the environment [2–4]. The combination of

global climate forces underlying human pressures threatens the fragile equilibrium required for a sustainable water supply and the good functioning of groundwater-dependent ecosystems (GDE) [5–7]. In many densely populated and irrigated drylands, external water transfer from other basins [8,9], and inner production of non-conventional resources such as urban wastewater reuse and seawater and brackish groundwater desalination to cope with water scarcity are being encouraged [10–12].

When water is used in urban areas for supply and in peri-urban areas for irrigation agriculture, water fluxes from these areas to regional groundwater bodies occur. The mechanisms for urban wastewater leaching are known. Buried urban sanitation infrastructure might not be watertight due to deterioration, and a fraction of wastewater may leach before reaching the urban wastewater treatment facility. Irrigated agriculture also entails an unavoidable loss of water during irrigation that may reach the aquifers. On favorable topographic and hydrogeological conditions, for instance when steep topography and low-permeability bedrock exist, urban and irrigation returns can be identified in water quantity and quality changes of local springs. Although these mechanisms are well known, the groundwater resource in most medium-sized urban and peri-urban areas is unknown because they are typically ungauged settings. Therefore, conceptualization of the hydrogeological functioning of these areas is crucial to understand and evaluate how these water fluxes can be used to alleviate the pressure on many stressed coastal groundwater bodies. However, geological exposure in urban areas is typically low to define aquifer geometry, especially in flat areas where geological exploration and groundwater monitoring is restricted to some geotechnical soundings and pumping wells at most. The opposite happens in towns with steep topography where geological formations and groundwater dynamics are partially observable and evaluations are possible. These evaluations may serve to conceptualize the groundwater resource generated in neighboring towns having similar habits for water consumption, but a flat topography that prevents direct groundwater observations.

Both steep topography and hydrogeological exposure are found in Adra town in southern Spain. Adra town is placed in a steep versant over small aquifers that contribute to the Adra River Delta Groundwater Body (ARDGB), which sustains GDEs, and includes a northern peri-urban area devoted to irrigation agriculture in greenhouses [13–15].

On the basis of existing or compiled datasets, the groundwater resource evaluation involves three general stages [16–18]: (1) Aquifer geometry and hydraulics definition, (2) conceptualization of the hydrogeological functioning, and (3) evaluation of the water balance components. This paper is aimed at developing the above two first general stages in deep, whilst the third one evaluates the groundwater resource contributed from the northern steep urban sector (NSUS) to the southern flat urban sector (SFUS), which belongs to the ARDGB.

For aquifer geometry definition, previous geological information [19] was revisited and near-surface geophysical techniques were applied. Near-surface geophysical techniques have been widely used in groundwater research to acquire basic information on aquifer geometry and some transient hydrogeological features [20–25]. This paper combines the Multichannel Analysis of Surface Waves (MASW) [26–32] and Ground Penetrating Radar (GPR) [33] techniques for these purposes. A basic Darcy’s Law formulation [34,35] was used to assess the NSUS groundwater discharge. For a fluent reading, the description for acronyms used is in Table 1.

Table 1. Description for acronyms used.

Acronym	Description
AGS	Actual groundwater storage
ARB	Adra River basin
ARD	Adra River Delta
ARDGB	Adra River Delta Groundwater Body

Table 1. Cont.

Acronym	Description
g1	Pleistocene colluvial 1
g2	Pleistocene colluvial 2
g3	Pleistocene colluvial 3
GDE	Groundwater-dependent ecosystem
GPR	Ground Penetrating Radar
MASW	Multichannel Analysis of Surface Waves
NSUS	Northern steep urban sector
PGS	Potential groundwater storage
SFUS	Southern flat urban sector
t1	Pleistocene littoral facies 1
t2	Pleistocene littoral facies 2
VE	Velocity of electromagnetic waves
VS	Shear-wave velocity
WB	Paleozoic weathered, fissured crystalline bedrock

2. Study Area

2.1. Location and Climate

Adra town ($36^{\circ}44'30''$ – $36^{\circ}45'30''$ N, $3^{\circ}00'$ – $3^{\circ}02'$ W) is located at the outlet of the Adra River basin (ARB) in the province of Almeria in southern Spain (Figure 1a). This coastal town has a surface of 1.82 km² and is crossed by small temporary streams that flow to the sea (Figure 1b). From a geomorphological point of view, these urban basins delimit a peri-urban area (2.64 km² in the 50–436 m a.s.l. elevation range) that influences the hydrology of a fraction of the urban area (0.97 km² in the 0–50 m a.s.l. elevation range) downstream [15]. The peri-urban area is divided into a southern sector (1.41 km² in the 50–150 m a.s.l. elevation range) devoted to irrigation agriculture in greenhouses and a northern sector (1.23 km² in the 150–436 m a.s.l. range) with low human influence (Figure 1c).

Climate is warm-summer Mediterranean according to the Köppen classification [36], which means a semiarid regime with hot dry summers and temperate rainy winters [14]. Insolation is high, 2900 h per year in low-lying places.

The 0.01° (~1-km) resolution nodal daily precipitation and temperature (maximum and minimum) series from the Iberia01 grid over the period 1971–2015 [37] was used to deduce weather conditions. Precipitation (P) occurs in three distinctive phases, each about four-month long as (1) a predominant rainy phase from October to January which represents around 50% of annual P; (2) a moderately rainy phase from February to May which means around 40% of annual P; and (3) a dry phase from June to September which records around 10% of annual P. Extreme rainfall events over 80 mm per day have been documented. Temperature (T) shows a bimodal distribution, each period about six-month long as (1) a warm period from May to October with average minimum and maximum monthly T of 15 °C in October and 31 °C in July, respectively; and (2) a temperate period from September to April with average minimum and maximum monthly T of 9 °C in January and 20 °C in April, respectively.

2.2. Geological and Hydrogeological Setting

The study area (Figure 1b) belongs to the Alpujarride tectonic complex from the Internal Domain of the Alpine Betic Cordillera [38,39]. The area is tectonically active as a consequence of the convergence between the African and Eurasian Plates, which ended with the collision of the Internal and External Betic domains during the early Miocene [39,40]. The combination of active tectonics and sea-level changes controls the accommodation space for Upper Miocene to present sedimentation [39,41].

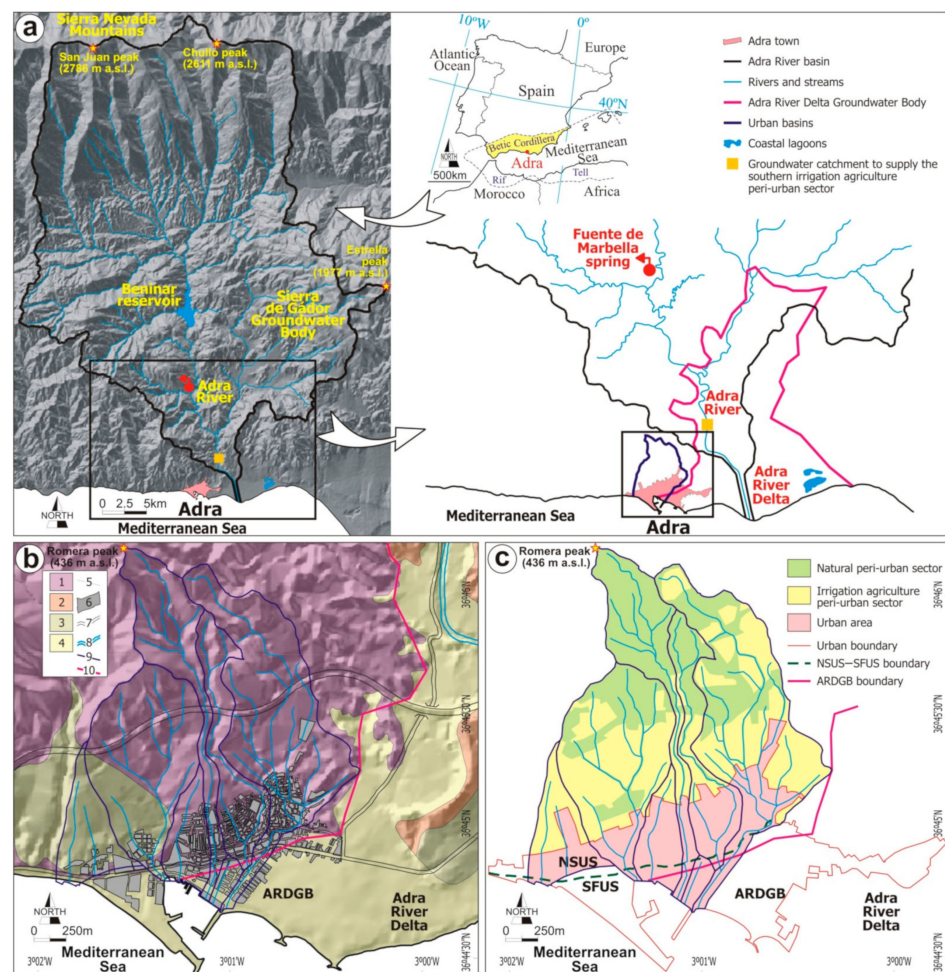


Figure 1. (a) Location of the study area in southern Spain, showing geographical sites cited in the text. (b) After the Geological Survey of Spain [38], the simplified 1:50,000-scale geological map of the urban and peri-urban areas; legend as (1) Paleozoic metamorphic formations, (2) Pliocene formations, (3) Pleistocene formations, (4) Holocene formations, (5) Undifferentiated geological contact, (6) Urban area, (7) Roads, (8) Adra River, (9) Urban basins, and (10) ARDGB boundary. (c) After the Andalusian Environmental Information Network [<http://www.juntadeandalucia.es/medioambiente/site/rediam>], the 1:25,000 scale land-use map of the urban basins, accessed on 15 January 2021.

Alcalá et al. (2002) [19] classified the geological record of Adra town into twelve geological formations attending to age, origin, and geometry. The two pre-orogenic formations included Paleozoic low- and medium-grade mica-schists and quartz-schists (crystalline bedrock). The ten post-orogenic formations included Pliocene to Quaternary sedimentary formations unconformably deposited over the bedrock (Figure 1b) as (1) a Pliocene deltaic formation; (2) five Pleistocene formations including two generations of littoral facies (t1 and t2) and colluvial (g1 and g2), and a cemented colluvial (g3); and (3) four Holocene formations including colluvial, the Adra River Delta (ARD) alluvial, present littoral facies, and anthropogenic filling. Direct field observations proved that the official 1:50,000-scale geological mapping [38] is detailed enough to explain the hydrogeological functioning in the peri-urban area (Figure 1b).

From a regional hydrogeological point of view, the eastern and southern sectors of Adra town are emplaced on the ARDGB, which is located at the ARB outlet (Figure 1a). The ARDGB has a surface of 49.2 km² and an average saturated thickness of 100 m. The average groundwater recharge and discharge are around 25 Mm³ year⁻¹ [14,42–44].

In the NSUS, Paleozoic weathered, fissured crystalline bedrock (WB), Pleistocene t1 and t2, and Holocene colluvial form a marginal aquifer not officially catalogued as a

groundwater body despite its historical relevance for water supply at homes and sparse traditional irrigated crops [15]. These formations are the subject of this paper.

2.3. Land Use and Water Allocation

In the area covered by the urban basins (Figure 1c), 1.29 km² is occupied by marginal rainfed crops, scrublands, and bare bedrock in the northern peri-urban sector, 1.41 km² is devoted to irrigation agriculture in greenhouses in the southern peri-urban sector, and 0.97 km² is urban area (Figure 1c). Irrigation agriculture in greenhouses is the main economic driver [13], which has attracted a new population in recent years. As a consequence, new urbanizations have occupied the fertile plain of the ARD in the eastern and southern sectors of the town (Figure 2). The Spanish National Institute for Statistics [45] reported around 20,000 inhabitants in the main urban area in 2019.

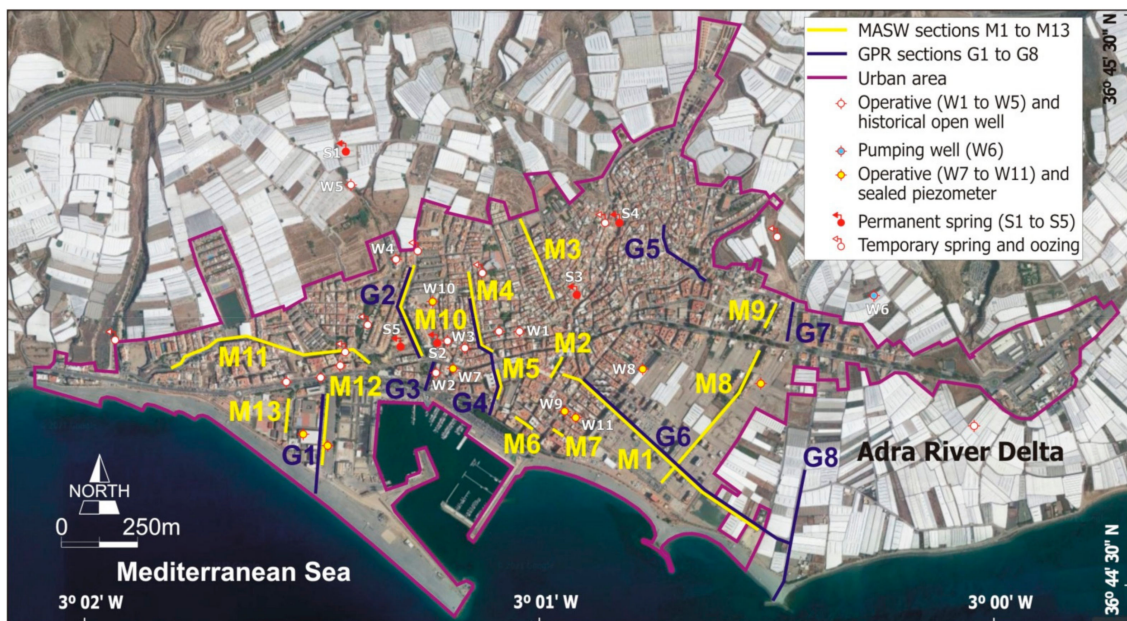


Figure 2. Satellite image of Adra town showing location of the MASW and GPR profiles, and selected groundwater observation points.

Water use is mostly devoted to urban and irrigation agriculture supply. Water allocation for urban supply is around 1.24 Mm³ per year; 0.97 Mm³ is intended to water supply at homes, 0.16 Mm³ to auxiliary industry and services, and 0.11 Mm³ to watering public gardens and urban cleaning. For 20,000 inhabitants, the average urban water endowment is 170 L per inhabitant and day [46]. Urban return from leakage in the sanitation network is around 0.20, after personal communication from the local water authority. Urban water allotment combines the ARD GW and the Fuente de Marbella spring from the Sierra de Gádor Groundwater Body in the mid-valley ARB (Figure 1a) [15]. In the peri-urban area, average water allocation for irrigation agriculture is around 7850 m³ per hectare and year, from which 1800 m³ are devoted to soil disinfestation in June when intensive crops rotate. Greenhouses produce vegetables (pepper, eggplant, cucumber, and similar others) in the winter–spring season, and melon and watermelon in the autumn–winter season. Irrigation is done through drip systems, which reduce evaporation and infiltration losses. Average irrigation efficiency is 0.85, thus the average irrigation return is 0.15 [47]. Irrigation water comes from groundwater pumped in the lower-valley Adra River alluviums, which belongs to the ARDWB (Figure 1a). Urban supply and irrigation agriculture do not use groundwater from local aquifers in the NSUS, although some abandoned handmade open wells evidence the historical use of this resource [15].

3. Methods

3.1. Aquifer Geometry Definition

3.1.1. Hydrogeological Field Surveys

Over the base of previous geological [19], hydrological [48], and hydrogeological [15] findings, and attending to the permeability type and storability reported by official reports [43,44,46], technical reports [49,50], and the scientific literature [14,42,51,52], the hydrogeological behavior of the geological formations is defined. Near-surface geophysical surveys (MASW and GPR) and new hydraulic tests to refine the geometry and hydrogeological functioning of the NSUS were performed. Two flash campaigns for piezometry and flow measurements in selected open wells (W1 to W6; Figure 2) and springs (S1 to S5; Figure 2) were carried out in September 2014 and June 2015. Piezometry used a level probe from Seba Hydrometrie with a precision of 0.005 m, whereas springs flow was measured manually 10-times to provide a confident average value.

3.1.2. MASW Technique

MASW is a seismic geophysical technique in which the Rayleigh wave fundamental mode dispersion curve and higher modes (if present) are extracted from a shot record and then inverted to generate a 1D VS [$L T^{-1}$] model [31,32]. This technique assesses the fundamental and higher modes simultaneously, thus permitting to obtain more accurate VS models [29,30]. A roll-along setup with a land-streamer acquisition system was used for data acquisition.

MASW data were acquired using a 24-channel SUMMIT II Compact Seismograph by DMT, Germany, with the following configuration: Recording array of 24 vertical component geophones, 2-m geophone spacing, 4-m separation between the source impact point and first geophone to minimize near-source effects, 2 stacks, 10-m displacement between readings, and a sampling rate of 0.25 ms. A Wacker Neuson BS60-4s vibratory rammer was used to generate the Rayleigh waves.

Data analysis was carried out with SurfSeis3 software[®] by the Kansas Geological Survey, The University of Kansas, USA. Data processing consisted of geometry edition, data filtering, muting (when needed), generation of overtones (frequency–time energy diagrams), and fundamental and higher modes (if present) identification. Finally, dispersion curves were determined and then subjected to a mathematical inversion process to obtain a continuous 2D VS model. Additional methodological details can be consulted in Martínez-Pagán et al. (2018) [53].

3.1.3. GPR Technique

GPR is an electromagnetic geophysical technique which uses transmitting and receiving antennas to record the time of propagation of the electromagnetic signal in the subsoil. In this study, the common or single offset antenna setup was used [33]. This technique provides radargrams, which are a set of radar traces, each representing the acquisition of the reflected signal in a point of the ground surface in time [54]. The propagation velocity of electromagnetic waves (VE) [$L T^{-1}$] and their amplitudes through the subsurface depends on the electrical and magnetic properties of geological materials and the adopted antenna frequency [55–58]. Penetration depth of the electromagnetic signal decreases as the clay content and salinity of the media and the antenna center frequency increase [33,55,58–61].

A GSSI SIR-3000 system equipment with a 270-MHz shielded antenna mounted on a cart with an encoder was used for data acquisition. The Reflexw software by Sandmeier was used for data processing. Relative dielectric permittivity was set to 10 according to near-surface subsoil characteristics, and later adjusted during processing. Processing flow consisted of time-zero correction, velocity refinement through comparison with well-known site features such as water table and bedrock depths, background removal, 1D filtering—bandpass butterworth filter maintaining the 70–400 MHz range, and topography handling. Additional methodological details can be consulted in Paz et al. (2007) [33].

3.2. Groundwater Resource Evaluation

In the NSUS, groundwater exploitation is virtually null, and groundwater discharge can be used as a reliable proxy of the groundwater resource contributed downstream. A basic Darcy’s Law formulation [34,35] for groundwater discharge was implemented, as:

$$D = -K dh/dl = i K b l, \tag{1}$$

where i is dimensionless hydraulic gradient; K is permeability expressed as the water flow traveled distance per time [$L T^{-1}$], in this case $m day^{-1}$; b is aquifer saturated thickness [L] in m; and l is aquifer discharge section [L] in m.

4. Results

4.1. Geophysical Data

4.1.1. MASW Survey

In February 2014, Martínez-Pagán et al. (2018) [53] completed thirteen MASW sections (labelled from M1 to M13, Figure 2). The MASW survey covered all the geological formations defined in Adra town. Basic data for all VS models were frequency in the 2.8–43.0 Hz range, phase velocity in the 259–1198 $m s^{-1}$ range, length from 40 m (section M7) to 810 m (section M1), and prospecting depth from 43 m (section M9) to 84 m (section M1). From active and passive MASW measurements, the 1D VS models were generated and interpolated to create 2D VS sections (called MASW sections) (Figure 3). The sections were topographically corrected. The vertical-equispaced VS values from all MASW sections were georeferenced and interpolated to create 2D VS layers at different elevations (called MASW maps) (Figure 4).

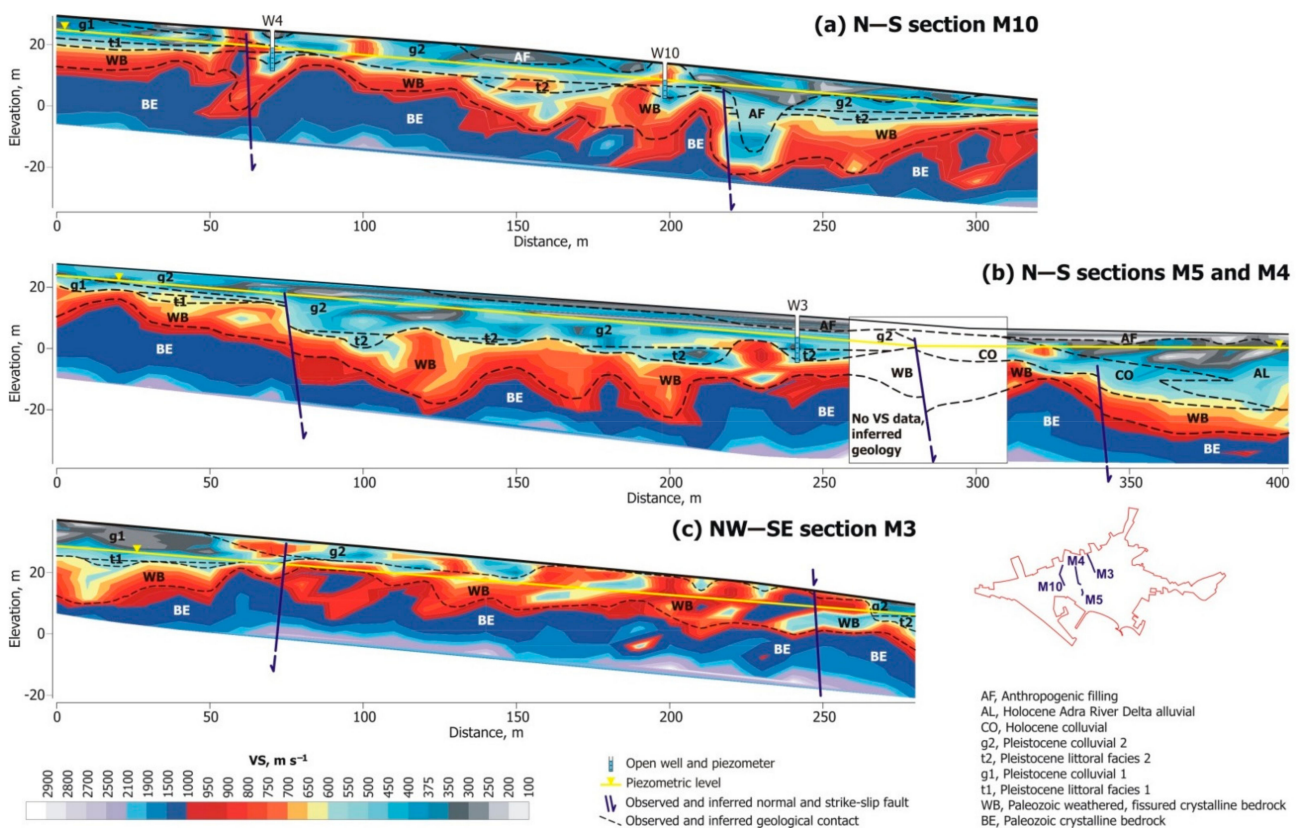


Figure 3. MASW sections M10, M4, M5, and M3; location is in Figure 2. A geological interpretation of VS values after Alcalá et al. (2002) [19] and the projected piezometric level after the flash campaign carried out in September 2014 are included; location of open well and piezometer W3, W4, and W10 is in Figure 2. Sections are topographically corrected and its vertical-to-horizontal scale ratio is 1:1.

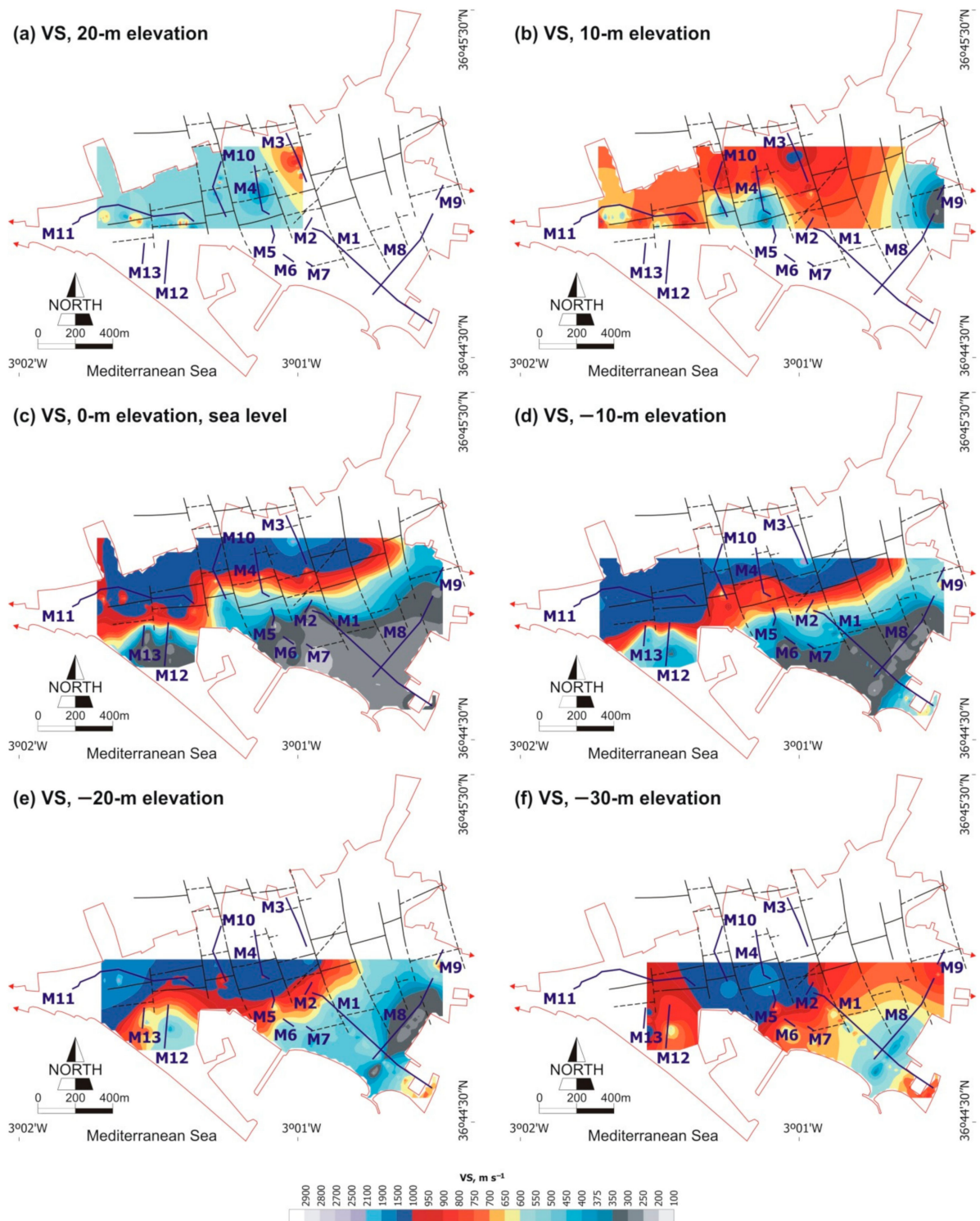


Figure 4. Some MASW maps at different elevation regarding the sea level in Adra town, showing observed and inferred normal and strike-slip fault systems, and location of MASW sections M1 to M13.

This paper uses the MASW sections and maps for geological definition following the interpretative criteria reported by Paz et al. (2020) [62]. These authors propose that VS propagation in sediments is a site-specific steady property determined by effective compaction and as such it is dependent on the age and depth of each geological material piled on vertical [63–66]. In Adra, the VS values obtained in previous studies [19,53,67] were $<350 \text{ m s}^{-1}$ for Holocene sediments, $350\text{--}600 \text{ m s}^{-1}$ for Pleistocene sediments, $600\text{--}900 \text{ m s}^{-1}$ for

Pliocene sediments, 900–1200 m s⁻¹ for WB, and >1200 m s⁻¹ for bedrock. Some sedimentary and tectonic processes can modify these ranges, such as cementation of coarse-grained sediments increasing VS up to 800 m s⁻¹ or high fissuring and weathering of the bedrock decreasing VS up to 700 m s⁻¹ [19,67]. For hydrogeological interpretation, the available geological and hydrogeological information was superimposed on sections M1 to M13. Four sections (M10, M4, M5, and M3) of special interest to deduce the hydrogeological functioning of the NSUS are displayed in Figure 3.

Sections M10 (Figure 3a), M4 (Figure 3b), and M3 (Figure 3c) show the NSUS, whereas section M5 (Figure 3b) shows the SFUS. Due to their continuity, sections M4 and M5 were interpreted together into a single section. A succinct description of these MASW sections is below. The uppermost 1–8 m thick VS < 300 m s⁻¹ is attributed to anthropogenic filling (sections M10, M4, M5, and M3), the underlying 2–10 m thick VS > 350 m s⁻¹ to Holocene colluvial and present littoral facies (section M5), the underlying 10–15 m thick 300 < VS < 600 m s⁻¹ to clay-rich g1 and g2 and coarse grained t1 and t2 (t1 is not identified in section M3), the underlying 5–10 m thick 600 < VS < 900 m s⁻¹ to cemented levels at the bottom of t1 and t2, the underlying 15–20 m thick 900 < VS < 1200 m s⁻¹ to WB, and the deeper VS > 1200 m s⁻¹ to the bedrock. This overall vertical VS distribution correlates well with the geological information, but some disruptions are observed. In M10, punctual VS < 300 m s⁻¹ underlying t2 is due to a dig gallery built in the 19th century to drain groundwater. In M10, M4, and M3, some patches embedded into g1 and g2 with VS > 1000 m s⁻¹ are attributed to isolated bedrock blocks. The pairs g1–t1 and g2–t2 show similar 300 < VS < 600 m s⁻¹, thus limiting identifications of the upper boundary of t1 and t2 forming aquifers regarding the lower boundary of g1 and g2 forming aquitards. The lowermost part of t1 and t2 and the uppermost part of WB are cemented and show similar VS < 900 m s⁻¹, thus preventing its boundary definition. As described in next Section 4.1.2, radargrams help to disambiguate these boundaries.

MASW maps (Figure 4) show how spatial VS continuity is interrupted by NW–SE normal and NE–SW strike-slip fault systems associated to active tectonics. The former is a first-order fault system determining the accommodation space for the Quaternary sedimentation whereas the latter is a second-order one that compartmentalizes the bedrock, thus inducing interruptions of some geological formations such as t1 and t2. The MASW maps identify geological boundaries of special hydrogeological interest, such as the (1) bedrock bathymetry at the 0-m (Figure 4c), –10-m (Figure 4d), and –20-m (Figure 4e) elevation maps; (2) NSUS–SFUS boundary at the 0-m (Figure 4c) and –10-m (Figure 4d) elevation maps; and (3) WB extension at the 10-m elevation map (Figure 4b).

4.1.2. GPR Survey

In June 2015, Paz et al. (2017) [33] completed eight GPR sections (labelled from G1 to G8, Figure 2). The GPR survey covered all the geological formations and coarsely followed the trace of the MASW sections to (1) disambiguate the boundary of geological structures having similar VS, such as the pairs t1–g1 and t2–g2; (2) deduce thickness of the shallowest anthropogenic filling; and (3) delineate transient hydrogeological features such as water table, capillary fringe, and seawater–freshwater interface. Basic data for all GPR sections were 50-Hz T-rate, 150-ns range, 120 scans per second, 40 scans per meter, 512 samples per scan, length from 88 m (section G3) to 652 m (section G6), and 4.5-m prospecting depth. Radargrams were topographically corrected and hydrogeological data were superimposed to refine shallow hydraulic features and geometry of the geological formations.

Three GPR sections (G2, G3, and G4) of special interest to deduce the hydrogeological functioning of the NSUS are displayed in Figure 5. In Adra, steep topography determines sub-horizontal reflections for Pleistocene sedimentation in the NSUS and horizontal ones for Holocene sedimentation in the SFUS. The southern sector of section G2 (Figure 5b) and the central sector of section G4 (Figure 5c) show how t2 produces stronger reflections than g2 due to cementation, thus permitting its identification. Outside the displayed sectors, the pair t1–g1 shows the same behavior. Bedrock and WB produce similar strong reflections,

thus limiting its boundary definition in some cases. Some shallow hydrogeological features are identified. An easily detected reflector inside the clay-rich g1 and g2 in G2 (Figure 5b) and G4 (Figure 5c) is capillary fringe, which narrowly follows piezometry measured in wells W1, W3, and W10 (Figure 2). This means that t1, t2, and the uppermost part of the WB together form an unconfined aquifer whose upward groundwater flow determines the capillary fringe position inside the clay-rich g1 and g2, which form an aquitard.

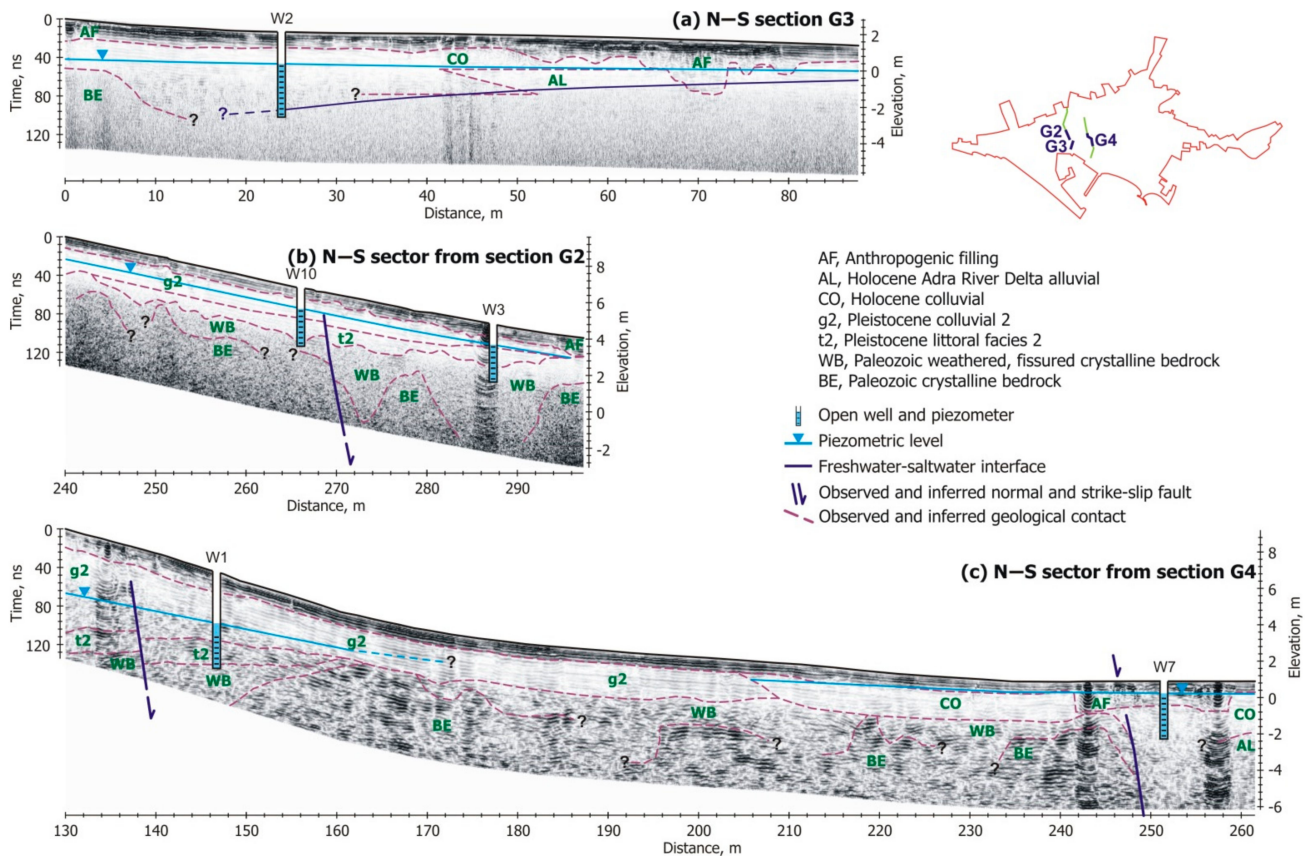


Figure 5. Selected sectors from GPR sections G2, G3, and G4 of especial hydrogeological interest; location is in Figure 2. The interpretation of radargrams was based on previous geological [19] and hydrogeological [15] data, and MASW sections (Figure 3). The projected piezometric level after the flash campaign carried out in June 2015 is included; location of open well and piezometer W1, W2, W3, W7, and W10 is in Figure 2. Profiles are topographically corrected and its vertical-to-horizontal scale ratio is 1:2.

In the SFUS, section G3 (Figure 5a) and the southern sector of section G4 (Figure 5c) show how the Holocene ARD Formation produces strong reflectors. In these coarse-grained sediments, the first strong reflection associated to the saturated media detection is stronger than the observed one in g1 and g2 and very closer to the water table, as deduced from piezometry measured in wells W2 and W7 (Figure 2), thus corroborating the unconfined behavior of this hydrogeological formation. In section G3 (Figure 5a), the VE signal loss below the sea level is attributed to the seawater–freshwater interface.

4.2. Hydrogeological Conceptualization

This section completes the two first goals of this paper, i.e., geometry and hydraulics definition of the geological formations in the NSUS. For geometry definition, geophysical findings, and previous [19] and new geological data were integrated on GIS to prepare the 1:5000 scale hydrogeological map of Adra town (Figure 6) and three representative hydrogeological cross-sections (Figure 7). For hydraulics definition, a permeability and effective porosity database was prepared from (1) compiled data from the literature de-

scribed in Section 3.1.1, which included official publications devoted to the Holocene ARD alluvial Formation in the SFUS, technical reports surveying the NSUS and SFUS, and scientific publications covering the NSUS and SFUS; and (2) data from specific field surveys in the NSUS, which included five double-ring infiltration tests in low-permeability formations, three pumping tests in open wells in high-permeability formations, and nine granulometric curves in different formations. On the basis of this information, the twelve geological formations have been classified into ten hydrogeological formations attending to the permeability type and storability (Table 2). The potential groundwater storage (PGS) of each hydrogeological formation is defined as the product of surface (direct and underlying outcrops), thickness (saturated and unsaturated), and effective porosity (Table 2). PGS must be considered a tentative magnitude of the maximum storability, not the actual storability. PGS has been calculated for all formations in the total urban area and for the existing ones in the NSUS.

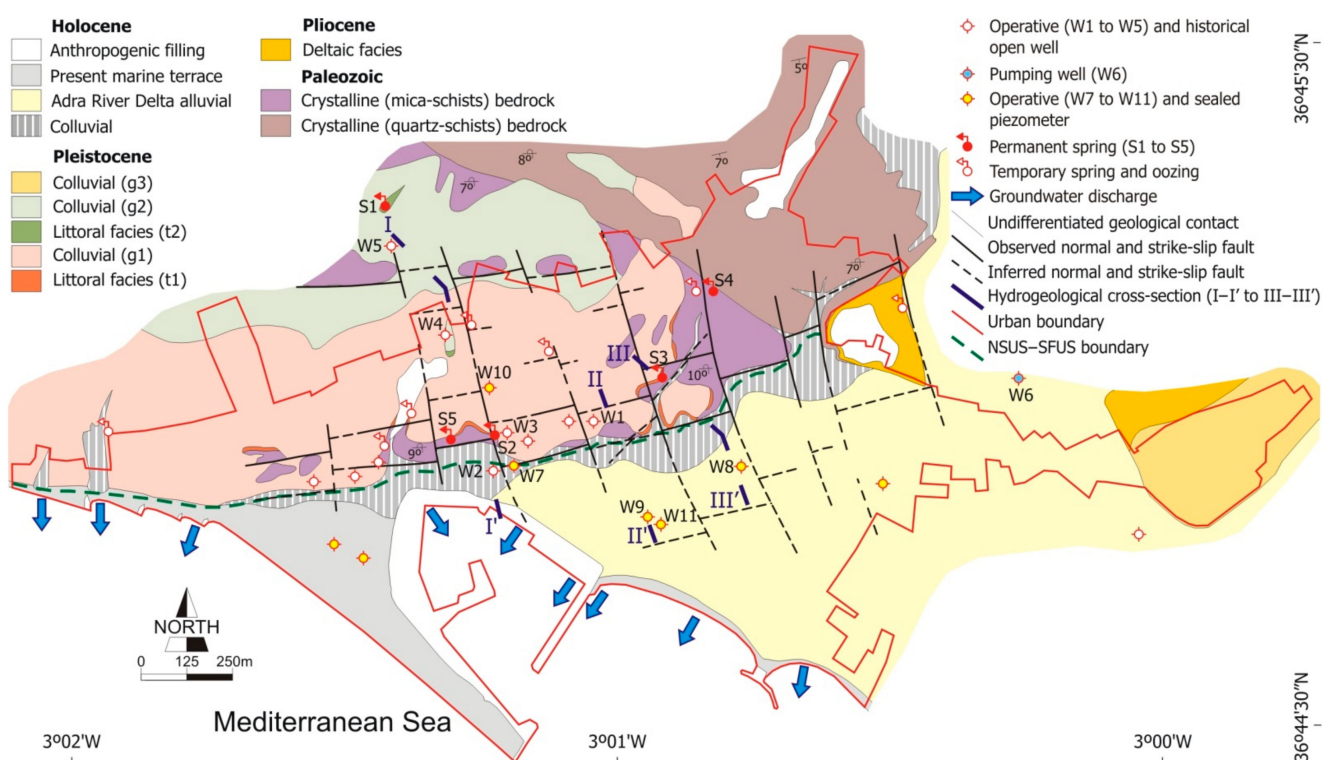


Figure 6. Hydrogeological map of Adra town at scale 1:5000, showing operative and historical groundwater observation points, sites where groundwater discharge to the sea is observable, and hydrogeological cross-sections I–I', II–II', and III–III' as in Figure 7.

The Paleozoic crystalline (mica-schists and quartz-schists) bedrock is a low-permeability formation constituting the impervious base of aquifers in the urban area (Table 2). This is catalogued as aquiclude. The MASW sections (Figure 3) and maps (Figure 4) delineate the bedrock geometry through $VS > 1200 \text{ m s}^{-1}$.

The WB Formation is a porous media forming a moderate- to high-permeability aquifer. In the NSUS, the surface is 0.68 km^2 , thickness is in the 1–18 m range, and its average PGS is around 0.27 Mm^3 (Table 2). The geometry of WB can be deduced through VS in the $800\text{--}1200 \text{ m s}^{-1}$ range from MASW sections (Figure 3) and maps (Figure 4). Recharge comes from direct rainfall and runoff infiltration, and urban and irrigation returns.

The Pliocene deltaic facies formation is unconformably deposited over the bedrock in the SFUS. This formation is catalogued as a moderate- to high-permeability aquifer (Figure 6) of 0.09 km^2 , thickness in the 4–31 m range, and average PGS around 0.03 Mm^3 (Table 2). Recharge comes from transference from the Holocene ARD alluvial formation.

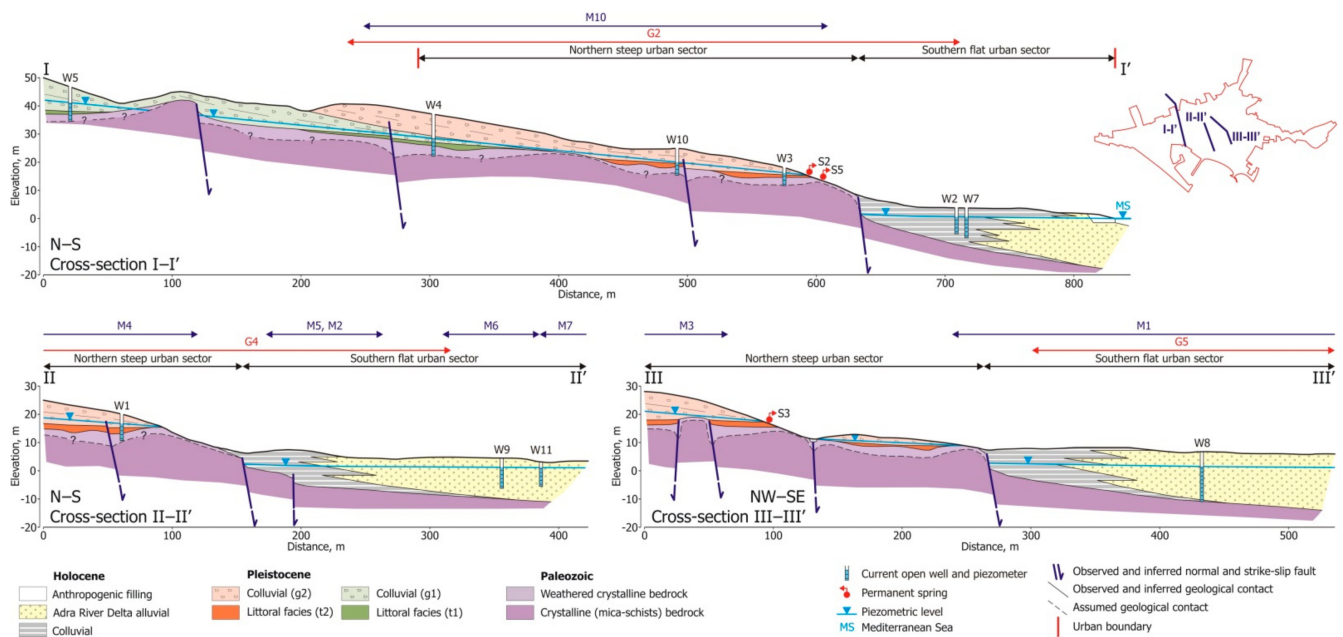


Figure 7. Three hydrogeological cross-sections I–I', II–II', and III–III' (see location in Figure 6), showing the distances covered by MASW (double sided arrow blue lines) and GPR (double sided arrow red lines) sections, operative and historical groundwater observation points, and the projected piezometric level after the flash campaign carried out in June 2015. Cross sections are topographically corrected, and its vertical-to-horizontal scale ratio is 1:2.

The Pleistocene record includes two littoral–continental sedimentary sequences in the NSUS and a continental sequence in the SFUS (Figure 6). A brief description is below.

In the NSUS, the two littoral–continental sequences are unconformably deposited over the bedrock (Figure 7). Each sequence includes littoral facies (t1 and t2) underlying clay-rich colluvial (g1 and g2) (Figures 6 and 7). t1 and t2 form a high-permeability aquifer of 0.41 km², thickness in the 1–8 m range, and average PGS around 0.21 Mm³ (Table 2). t1 and t2 are hydraulically connected to WB and partially disconnected between them, as deduced from the studied MASW (Figure 3) and GPR (Figure 5) sections. The normal and strike-slip fault systems compartmentalize t1 and t2, but do not interrupt apparently the continuity of WB, as deduced from the 10-m elevation MASW map (Figure 4b). The result is groundwater flowing throughout WB, t1, and t2, thus forming together a confined aquifer in the NSUS. Geometry, piezometry in open wells, and groundwater discharge in springs at different elevations corroborate this confined hydraulic behavior (Figure 7). This aquifer is hydraulically connected (and discharges) to the unconfined Holocene ARD alluvial formation. Recharge comes from direct rainfall and runoff infiltration, and urban and irrigation returns. g1 and g2 are low-permeability formations catalogued as aquitards that confine t1 and t2, respectively (Figures 6 and 7). Surface is 0.58 km², thickness is in the 1–32 m range, and its average PGS is around 0.04 Mm³ (Table 2).

In the SFUS, the third Pleistocene continental sequence includes a cemented colluvial (g3) unconformably deposited over the Pliocene deltaic facies Formation. This is a moderate- to low-permeability formation catalogued as an aquitard (Figure 6). Surface is 0.10 km², thickness is in the 1–29 m range, and its average PGS is around 0.03 Mm³ (Table 2). Recharge comes from direct rainfall and runoff infiltration, and transference from the Holocene ARD alluvial formation.

The Holocene sedimentary record includes four formations: Colluvial, ARD alluvial, present littoral facies, and anthropogenic filling. A brief description is below.

The colluvial formation is emplaced on the NSUS–SFUS boundary unconformably deposited over the bedrock and the pair t2–g2 (Figures 6 and 7). It is catalogued as a moderate- to high-permeability aquifer. In the NSUS, surface is 0.11 km², thickness is in the 1–21 m range, and its average PGS is around 0.07 Mm³ (Table 2). Recharge comes from

discharge from upstream hydrogeological formations, direct rainfall and runoff infiltration, and urban return. Discharge is done to the Holocene ARD alluvial formation and the sea.

The ARD alluvial Formation is in the SFUS and belongs to the ARDGB. It is cataloged as a high-permeability aquifer (Figure 6). The surface is 0.59 km², thickness is in the 1–35 m range, and its average PGS is around 0.78 Mm³ (Table 2). Recharge comes from upstream infiltration in the Adra River valley alluviums, and irrigation and urban returns. Discharge is produced by pumping, transference to other hydrogeological formations, and to the sea.

The present littoral facies formation is in the SFUS and results from civil works to prevent coastal erosion [19]. Only the western beaches have hydrological interest, forming a shallow high-permeability aquifer of 0.17 km², thickness in the 1–9 m range, and average PGS of around 0.09 Mm³ (Table 2). Recharge comes from rainfall and runoff infiltration, and discharge from other upstream hydrogeological formations.

The anthropogenic filling formation appears as high-permeability patches that contribute to urban runoff or groundwater storage when overlying low- or high-permeability formations, respectively. In the NSUS, surface is 0.05 km², thickness is in the 1–6 m range, and the average PGS is around 0.03 Mm³ (Table 2). Recharge comes from rainfall and runoff infiltration, and urban return.

4.3. Groundwater Resource Evaluation

This section completes the third goal of this paper, i.e., the groundwater resource evaluation in the NSUS. Excluding formations behaving as aquicludes (bedrock) and aquitards (g1, g2, and g3), the average PGS in Adra town is around 1.77 Mm³. This figure varies in the 0.12–5.49 Mm³ range when the minimum and maximum thickness and effective porosity values are used (Table 2). In the NSUS, g1 and g2 confine the aquifer formed by WB, t1, and t2. Excluding bedrock, g1, and g2, average PGS is around 0.58 Mm³ and its range is 0.05–1.71 Mm³ (Table 2). The actual groundwater contribution to the SFUS must be less than average PGS, which is the theoretical maximum value.

Since groundwater exploitation is virtually null, the NSUS groundwater discharge can be considered a reliable proxy of the groundwater contributed from the NSUS to the SFUS. For groundwater discharge evaluation through the Darcy's Law formulation, the hydrogeological formations in the NSUS were grouped into three aquifers (1) that formed by WB, t1, and t2 (called NSUS aquifer); (2) the northern sector of the colluvial formation; and (3) the anthropogenic filling patches. In each aquifer, input data were saturated thickness, discharge section, hydraulic gradient, and permeability (Table 3).

Average saturated thickness is total thickness minus the difference in topography and piezometry deduced from open wells and springs. Average saturated thickness of the NSUS aquifer is around 0.85-fold the average total thickness described in Table 2. This figure results from weighting full-saturated aquifer sectors such as those shown in the hydrogeological cross-sections I–I' to III–III' (Figure 7) and others fully desaturated. Average saturated thickness of colluvial and anthropogenic filling formations are 0.7- and 0.5-fold the average total thickness, respectively. The aquifer discharge sections were deduced from the hydrogeological map (Figure 6). The desaturated aquifer sectors were excluded from this calculation.

After the two flash campaigns carried out in September 2014 and June 2015, piezometry in open wells W1 to W6 (Figure 2) and groundwater discharge elevation in springs S1 to S5 (Figure 2) were used to delineate the piezometric level and define the hydraulic gradient. Average hydraulic gradients varied in the 0.017–0.044 range and coarsely followed the topographic gradient as 0.035 in the NSUS aquifer, 0.017 in the colluvial formation, and 0.004 in the anthropogenic filling formation (Table 3). Average permeability for these formations is in Table 2.

Table 2. Geometry, hydraulics data, and potential groundwater storage (PGS) of the hydrogeological formations in the total urban area and the NSUS.

Age	Hydrogeological Formation	Main Lithology	Urban Surface, km ^{1,2}	NSUS Surface, km ^{1,2}	Thickness, m ²	Permeability, m day ⁻¹ ³	Effective Porosity, ³	PGS in the Urban Area, Mm ^{3,4}	PGS in the NSUS, Mm ^{3,4}	Hydraulic Behavior
Paleozoic	Bedrock	Mica-schists, quartz-schists	1.82	0.77	–	–	–	–	–	Aquiclude
	Weathered, fissured bedrock	Mica-schists, quartz-schists	0.86	0.68	1–18 (8)	0.9–1.5 (1.1) n = 3	0.02–0.07 (0.05) n = 3	0.02–1.08 (0.34)	0.01–0.86 (0.27)	Aquifer
Pliocene	Deltaic facies	Sand, gravel, silt	0.09	–	4–31 (17)	1.1–5.2 (2.9) n = 3	0.01–0.05 (0.02) n = 3	<0.01–0.14 (0.03)	–	Aquifer
Pleistocene	Littoral facies (t1, t2)	Gravel, sand	0.41	0.41	1–8 (4)	2.3–9.3 (4.2) n = 4	0.06–0.17 (0.13) n = 4	0.03–0.56 (0.21)	0.03–0.53 (0.21)	Aquifer
	Detrital colluvial (g1, g2)	Gravel, sand, clay	0.58	0.58	1–32 (9)	0.05–0.09 (0.07) n = 3	<0.01–0.01 (<0.01) n = 3	<0.01–0.20 (0.04)	<0.01–0.20 (0.04)	Aquitard
	Cemented colluvial (g3)	Cemented gravel, sand	0.10	–	1–29 (14)	0.12–0.44 (0.28) n = 2	0.01–0.03 (0.02) n = 2	<0.01–0.09 (0.03)	–	Aquitard
Holocene	Adra River Delta alluvial	Sand, silt	0.35	0.11	1–21 (9)	0.8–2.9 (1.4) n = 3	0.05–0.10 (0.07) n = 3	0.02–0.74 (0.22)	<0.01–0.23 (0.07)	Aquifer
	Present littoral facies	Sand	0.59	–	1–35 (19)	5.3–30.7 (13.8) n = 6	0.04–0.12 (0.07) n = 6	0.02–2.48 (0.78)	–	Aquifer
	Colluvial	Gravel, sand, clay	0.17	–	1–9 (4)	5.1–30.3 (14.5) n = 4	0.08–0.17 (0.13) n = 4	0.01–0.26 (0.09)	–	Aquifer
	Anthropogenic filling	Blocks, sand, silt	0.17	0.05	1–6 (3)	5.2–8.2 (6.7) n = 2	0.14–0.23 (0.17) n = 2	0.02–0.24 (0.09)	<0.01–0.07 (0.03)	Aquifer

¹ Surface of Adra town is 1.82 km² and surface of the NSUS is 0.77 km². Surface of each hydrogeological formation is the sum of direct and underlying outcrops deduced from the 1:5000 scale hydrogeological map (Figure 6) and cross-sections (Figure 7), geotechnical sounding data, MASW sections (Figure 3) and maps (Figure 4), and GPR sections (Figure 5). ² Thickness is deduced from direct field observations, geotechnical sounding data, and geophysical surveys; in parenthesis is the average value calculated on GIS. ³ Permeability and effective porosity data come from the compiled data from the literature described in Section 3.1.1 and the specific field surveys described in Section 4.2; in parenthesis is the average value; n is the number of data. ⁴ PGS is the product of surface, thickness (saturated and unsaturated), and effective porosity of each hydrogeological formation; in parenthesis is the average value.

Table 3. NSUS groundwater discharge after the Darcy's Law formulation.

Hydrogeological Formation ¹	i^2	K^2	b^2	l^2	D^2	AGS^2
Weathered, fissured bedrock	0.035	0.9–1.5 (1.1) n = 3	0.8–15.3 (6.8)	1860	0.02–0.55 (0.18)	0.01–0.73 (0.23)
Littoral facies (t1, t2)	0.035	2.3–9.3 (4.2) n = 4	0.8–6.8 (3.4)	450	0.01–0.36 (0.08)	0.02–0.47 (0.18)
Detrital colluvial (g1, g2)	0.035	0.05–0.09 (0.07) n = 3	0.5–16.0 (4.5)	1610	<0.01–0.03 (<0.01)	<0.01–0.10 (0.02)
Colluvial	0.017	0.8–2.9 (1.4) n = 3	0.6–12.6 (5.4)	480	<0.01–0.11 (0.02)	<0.01–0.14 (0.04)
Anthropogenic filling	0.004	5.2–8.2 (6.7) n = 2	0.5–3.0 (1.5)	110	<0.01	<0.01–0.03 (0.01)

¹ In Table 2, age, lithological description, and PGS of each hydrogeological formation. ² i = average dimensionless hydraulic gradient; K = permeability in m day^{-1} (Table 2); b = aquifer saturated thickness in m; l = aquifer discharge section in m; D = NSUS groundwater discharge in $\text{Mm}^3 \text{ year}^{-1}$; and AGS = actual groundwater storage in Mm^3 as the product of b , surface (Table 2), and effective porosity (Table 2). K , b , D , and AGS include range and average value into parenthesis.

Excluding g1 and g2 behaving as aquitards, the average NSUS groundwater discharge is around $0.28 \text{ Mm}^3 \text{ year}^{-1}$. This figure varies in the $0.03\text{--}1.02 \text{ Mm}^3 \text{ year}^{-1}$ range when the minimum and maximum values of saturated thickness and permeability are considered (Table 3). Average actual groundwater storage (AGS), which is expressed as the product of surface (direct and underlying outcrops as in Table 2), saturated thickness, and effective porosity (Table 2), is around 0.47 Mm^3 (Table 3).

NSUS groundwater discharge was compared to groundwater recharge produced from precipitation in the peri-urban area (2.64 km^2) and NSUS (0.77 km^2), irrigation return in the southern peri-urban sector devoted to irrigation agriculture in greenhouses (1.41 km^2), and urban return in the NSUS (Table 4). Using tracer and physical techniques, Alcalá et al. (2008) [15] tentatively evaluated the average recharge rate from precipitation in the peri-urban and urban areas as 10 mm year^{-1} . This figure is similar to that reported by Andreu et al. (2011) [68] in coastal areas in southern Almería province. The average recharge from precipitation is $0.03 \text{ Mm}^3 \text{ year}^{-1}$. As described in Section 2.3, average water allocation for urban supply is $1.24 \text{ Mm}^3 \text{ year}^{-1}$ [46]. After checking a similar inhabitant density along the main urban area, this figure was linearly approached as $0.52 \text{ Mm}^3 \text{ year}^{-1}$ for the 0.77-km^2 NSUS. Applying the urban return coefficient of around 0.20 informed by the local water authority, the urban return contributing to recharge is around $0.10 \text{ Mm}^3 \text{ year}^{-1}$. Average water allocation for irrigation agriculture is around 7850 m^3 per hectare and year and the average irrigation return coefficient is 0.15 [47]. The irrigation return contributing to recharge is around $0.17 \text{ Mm}^3 \text{ year}^{-1}$ (Table 4). Average groundwater recharge is around $0.31 \text{ Mm}^3 \text{ year}^{-1}$ (Table 4). This figure is $0.03 \text{ Mm}^3 \text{ year}^{-1}$ higher than average groundwater discharge.

Table 4. Groundwater recharge in the NSUS.

Recharge Component	Area Covered ¹	Surface, km^2	Recharge, $\text{Mm}^3 \text{ year}^{-1}$	Reference
Precipitation	PUA, NSUS	3.41	0.03	[15]
Urban return	NSUS	0.77	0.10	[46]
Irrigation return	SPUS	1.41	0.17	[47]

¹ PUA = peri-urban area; NSUS = northern steep urban sector; SPUS = southern peri-urban area devoted to irrigation agriculture in greenhouses.

5. Discussion

5.1. The MASW Technique for Geological Definition

The MASW technique has widely been used in seismic hazard research, especially in urban areas [29–32,53,69]. The experience in shallow groundwater research is incipient [26–28] and has mostly focused to disambiguate geological structures when other

near-surface geophysical techniques fail to obtain a reliable interpretation [26,27,62]. This paper widens the experience in shallow groundwater research to define the geometry of geological structures once reference VS values are available. In Adra town, the confident use of the MASW technique had the VS values assigned to each geological formation in previous research [19,53,67], e.g., $VS > 1200 \text{ m s}^{-1}$ for Paleozoic bedrock, $800\text{--}1200 \text{ m s}^{-1}$ for WB, $500\text{--}900 \text{ m s}^{-1}$ for Pliocene deltaic facies, $350\text{--}600 \text{ m s}^{-1}$ for Pleistocene formations, and $<350 \text{ m s}^{-1}$ for Holocene formations.

However, the MASW technique must be used together with other near-surface geophysical techniques relying on other subsurface properties other than VS in order to solve potential constraints imposed by the possible similar VS response of different geological structures. For instance, g1 and g2 show similar VS values than t1 and t2 (Figure 3), meaning a handicap at defining the geometry of the confined NSUS aquifer formed by WB, t1, and t2 (Figure 7). Adra town is a low-resistivity coastal area having high environmental salinity and clay-rich formations such as g1 and g2, so the geophysical electrical techniques do not seem to be suitable for disambiguating the pairs g1–t1 and g2–t2. The GPR technique was chosen to disambiguate these structures having similar VS values, as well as to identify key hydrogeological features, such as piezometric level, capillary fringe, and seawater–freshwater interface (Figure 5). MASW provides higher exploration depths than GPR, but less detailed resolution, whereas GPR is highly responsive to detailed subsurface electrical and magnetic changes related to natural and human-induced geological and hydrological heterogeneities [33,55,58–60].

This paper introduces a novelty in VS data post-treatment. Several vertical-equispaced MASW maps from -35-m to 30-m elevation regarding the sea level were created to identify continuity of the geological structures. This VS data post-treatment has enabled us to display where and why the boundary between the bedrock and the Pliocene to Quaternary sedimentary formations changes at different depths, for instance, abruptly due to normal and strike-slip fault systems or smoothly due to sedimentary processes (Figure 4). The bedrock bathymetry determines the accommodation space for sedimentary formations forming aquifers. These applications are of particular interest in urban areas where the capability for direct subsoil observations is typically quite limited. In Adra town, MASW sections (Figure 3) and maps (Figure 4) helped to create the 1:5000 scale hydrogeological map (Figure 6) and cross-sections I–I' to III–III' (Figure 7). This paper proposes the MASW technique for geological definition in urban shallow groundwater research, taking into account that other techniques to solve possible constraints imposed by the explored media features may be needed.

5.2. Use of the Groundwater Resource

The sources and mechanisms for groundwater recharge and discharge in urban areas are more numerous and complex than in natural environments, as documented many urban groundwater research [70–75]. Buildings and civil works combine with human-made drainage networks, sanitation systems, and paving to introduce new recharge and discharge components or modify the existing ones. In Adra town, this problematic increase because the study area must be extended to include a peri-urban area devoted to natural uses and irrigation agriculture that influences the urban hydrology downstream. In the NSUS, irrigation ($0.17 \text{ Mm}^3 \text{ year}^{-1}$) and urban ($0.10 \text{ Mm}^3 \text{ year}^{-1}$) returns are clearly higher than the recharge from precipitation ($0.03 \text{ Mm}^3 \text{ year}^{-1}$). The consequence is an uncatalogued groundwater resource contributing to the SFUS. The ARDGB, where the SFUS is emplaced, provides most of the usable water, sustains some GDEs catalogued in the Ramsar Convention list [14], and is officially protected to avoid new exploitations [43,44,46]. However, the NSUS and the southern irrigation agriculture peri-urban sector form a not officially catalogued marginal hydrogeological system that contributes to the SFUS and therefore to the ARDGB. This groundwater resource discharges to the sea under Adra town. This paper conceptualizes the functioning of this marginal hydrogeological system and

provides a preliminary evaluation of the groundwater resource contributed to the SFUS. This resource could sustainably be exploited downstream.

Average groundwater discharge is around $0.28 \text{ Mm}^3 \text{ year}^{-1}$, and may vary in the $0.03\text{--}1.02 \text{ Mm}^3 \text{ year}^{-1}$ range when the minimum and maximum values of saturated thickness and permeability are considered (Table 3). Average aquifer recharge is around $0.31 \text{ Mm}^3 \text{ year}^{-1}$. As expected in unexploited aquifers, the magnitude of average groundwater discharge and recharge in the NSUS is similar and lower than the calculated AGS of around 0.47 Mm^3 (Table 3). Three conclusions regarding the conceptualization of the NSUS aquifer functioning are gained: (1) The recharge-to-discharge absolute difference is $0.03 \text{ Mm}^3 \text{ year}^{-1}$, so other sources and mechanisms for groundwater discharge probably occur and must be characterized, for instance occasional groundwater pumping to lower the piezometric level during building construction, groundwater up-take by phreatophytes and deep-rooted vegetation, and direct groundwater evaporation in sites having a quite shallow piezometry; (2) average saturated thickness is about 0.5–0.9-fold the total thickness of the hydrogeological formations, but there are desaturated sectors that must be characterized; and (3) renewability of the groundwater resource is high enough to sustain a durable small exploitation downstream, as deduced from an average groundwater turnover time less than one year, here tentatively expressed by means of the groundwater recharge ($0.31 \text{ Mm}^3 \text{ year}^{-1}$; Table 4) to AGS (0.47 Mm^3 ; Table 3) ratio [76,77]. This exploitation may guarantee the permanent water supply to watering public gardens and urban cleaning, currently around 0.11 Mm^3 per year and tending to increase in coming years as new urbanized areas are being planned. Other ecological uses could be also considered.

Other hydrogeological gaps to resolve in future research are (1) definition of the hydraulic behavior of fault as water-bearing or water-tight, (2) characterization of the hydraulic effect of civil works on groundwater flow, and (3) how climate change and subsequent land-use adaptations can affect this groundwater resource.

6. Conclusions

The favorable climate in the Mediterranean coastal area has potentiated an increasing urbanization and occupation of peri-urban areas for profitable irrigation agriculture. The new land uses and water demands have evidenced the controversy of having a scarce conventional water resource, while the intensive water use generates a difficult-to-manage non-conventional water resource that may complement the conventional one. In the context of global change and growing water demands, the small marginal aquifers in urban and peri-urban areas may play a role in complementing the urban allotment for specific uses. The smart cities in the near future will consider new paradigms for sustainability such as “water recycling and reusing”.

Adra town in southern Spain was the case study chosen to show this problematic and introduce a feasible methodology to conceptualize the NSUS aquifer functioning and provide a tentative magnitude of the groundwater resource contributed to the SFUS. For this, findings from the geological, geophysical, hydrological, and hydrogeological surveys were combined to create a 1:5000 scale hydrogeological map and cross-sections, which are basic tools to design a proper urban water planning. The MASW and GPR geophysical techniques were especially useful for aquifer geometry definition. The NSUS average groundwater discharge was evaluated around $0.28 \text{ Mm}^3 \text{ year}^{-1}$. Among other uses, this resource may guarantee a permanent water supply to watering public gardens and urban cleaning, which is currently around $0.11 \text{ Mm}^3 \text{ year}^{-1}$ and will increase due to new urbanized areas, thus alleviating the pressure on the ARDGB.

This paper seeks to offer a feasible methodology for groundwater research in medium-size urban areas having steep topography, low-permeability bedrock underlying shallow urban aquifers, and peri-urban areas influencing the urban hydrology. The authors found that the introduced basic formulation for groundwater discharge enables for a tentative evaluation of this resource at most. For this reason, solving of the discussed hydrogeological

gaps and designating of suitable sites for a sustainable groundwater exploitation regime will be subjects of future research.

Author Contributions: Conceptualization, F.J.A.; methodology, F.J.A., P.M.-P., M.C.P., and M.N.; formal analysis, P.M.-P., M.C.P., J.P.-C., and M.N.; data curation, M.C.P. and J.P.-C.; writing—original draft preparation, F.J.A.; writing—review and editing, F.J.A., P.M.-P., M.C.P., M.N., and F.D.; project administration, F.J.A.; funding acquisition, M.N. and F.D. All authors have read and agreed to the published version of the manuscript.

Funding: This research was partly supported by the Spanish Research Projects CGL2016-78075-P and CGL2007-66745-C02-02/BTE, and the Andalusian Research Projects IE17_5560_EEZA and P06-RNM-01732, all including European Regional Development Funds.

Institutional Review Board Statement: Not applicable.

Informed Consent Statement: Not applicable.

Data Availability Statement: The data presented in this study are available on request from the corresponding author.

Acknowledgments: The authors are grateful for the information on the urban and irrigation water supply systems provided by the Water Authority of Adra town and local Water Users Associations, respectively. Jorge M. Carvalho from University of Porto is also acknowledged for providing GPR equipment and software. The valuable comments and suggestions by two anonymous referees are greatly appreciated.

Conflicts of Interest: The authors declare no conflict of interest.

References

1. Sabater, S.; Barceló, D. *Water Scarcity in the Mediterranean. Perspectives Under Global Change*; Springer: Berlin/Heidelberg, Germany, 2010. [[CrossRef](#)]
2. Custodio, E. Coastal aquifers of Europe: An overview. *Hydrogeol. J.* **2010**, *18*, 269–280. [[CrossRef](#)]
3. Dalin, C.; Wada, Y.; Kastner, T.; Puma, M.J. Groundwater depletion embedded in international food trade. *Nature* **2017**, *543*, 700–704. [[CrossRef](#)] [[PubMed](#)]
4. Custodio, E.; Andreu-Rodes, J.M.; Aragón, R.; Estrela, T.; Ferrer, J.; García-Aróstegui, J.L.; Manzano, M.; Rodríguez-Hernández, L.; Sahuquillo, A.; Del Villar, A. Groundwater intensive use and mining in south-eastern peninsular Spain: Hydrogeological, economic and social aspects. *Sci. Total Environ.* **2016**, *559*, 302–316. [[CrossRef](#)] [[PubMed](#)]
5. Martínez-Valderrama, J.; Ibáñez, J.; Alcalá, F.J. AQUACOAST: A simulation tool to explore coastal groundwater and irrigation farming interactions. *Sci. Program.* **2020**, *2020*, 9092829. [[CrossRef](#)]
6. Alcalá, F.J.; Martínez-Valderrama, J.; Robles-Marín, P.; Guerrero, F.; Martín-Martín, M.; Raffaelli, G.; Tejera de León, J.; Asebriy, L. A hydrological-economic model for sustainable groundwater use in sparse-data drylands: Application to the Amtoudi Oasis in southern Morocco, northern Sahara. *Sci. Total Environ.* **2015**, *537*, 309–322. [[CrossRef](#)]
7. Alcalá, F.J.; Martín-Martín, M.; Guerrero, F.; Martínez-Valderrama, J.; Robles-Marín, P. A feasible methodology for groundwater resource modelling for sustainable use in sparse-data drylands: Application to the Amtoudi Oasis in the northern Sahara. *Sci. Total Environ.* **2018**, *630*, 1246–1257. [[CrossRef](#)]
8. Morote, Á.F.; Olcina, J.; Rico, A.M. Challenges and proposals for socio-ecological sustainability of the tagus–segura aqueduct (Spain) under climate change. *Sustainability* **2017**, *9*, 2058. [[CrossRef](#)]
9. Morote, Á.F.; Olcina, J.; Hernández, M. The use of non-conventional water resources as a means of adaptation to drought and climate change in Semi-Arid Regions: South-Eastern Spain. *Water* **2019**, *11*, 93. [[CrossRef](#)]
10. Licciardello, F.; Milani, M.; Consoli, S.; Pappalardo, N.; Barbagallo, S.; Cirelli, G. Wastewater tertiary treatment options to match reuse standards in agriculture. *Agric. Water Manag.* **2018**, *210*, 232–242. [[CrossRef](#)]
11. Allam, A.R.; Saaf, E.J.; Dawoud, M.A. Desalination of brackish groundwater in Egypt. *Desalination* **2002**, *152*, 19–26. [[CrossRef](#)]
12. Alcalá, F.J. Usefulness of the Cl/Br ratio to identify the effect of reverse osmosis treated waters on groundwater systems. *Desalination* **2019**, *470*, 114102. [[CrossRef](#)]
13. Downward, S.R.; Taylor, R. An assessment of Spain's Programa AGUA and its implications for sustainable water management in the province of Almería, southeast Spain. *J. Environ. Manag.* **2007**, *82*, 277–289. [[CrossRef](#)]
14. Rodríguez-Rodríguez, M.; Benavente, J.; Alcalá, F.J.; Paracuellos, M. Long-term water monitoring in two Mediterranean lagoons as an indicator of land-use changes and intense precipitation events (Adra, Southeastern Spain). *Estuar. Coast. Shelf Sci.* **2011**, *91*, 400–410. [[CrossRef](#)]
15. Alcalá, F.J.; Solé, A.; Creus, C.; Domingo, F. Aporte urbano de agua subterránea hacia masas hídricas regionales y ecosistemas dependientes. Caso de la localidad costera de Adra (SE de España). In *VII Simposio del Agua en Andalucía*, 1st ed.; López-Geta, J.A., Rubio, J.C., Martín-Machuca, M., Eds.; Geological Survey of Spain: Madrid, Spain, 2008; Volume 2, pp. 699–708.

16. Poeter, E.; Anderson, D. Multimodel ranking and inference in ground water modeling. *Groundwater* **2005**, *43*, 597–605. [CrossRef]
17. Hojberg, A.L.; Refsgaard, J.C. Model uncertainty-parameter uncertainty versus conceptual models. *Water Sci. Technol.* **2005**, *52*, 177–186. [CrossRef]
18. Beven, K. Towards integrated environmental models of everywhere: Uncertainty, data and modelling as a learning process. *Hydrol. Earth Syst. Sci.* **2007**, *11*, 460–467. [CrossRef]
19. Alcalá, F.J.; Espinosa, J.; Navarro, M.; Sánchez, F.J. Propuesta de división geológica de la localidad de Adra (provincia de Almería). Aplicación a la zonación sísmica. *Rev. Soc. Geológica España* **2002**, *15*, 55–66.
20. Monteiro Santos, F.A.; Sultan, S.A.; Represas, P.; El Sorady, A.L. Joint inversion of gravity and geoelectric data for groundwater and structural investigation: Application to the northwestern part of Sinai, Egypt. *Geophys. J. Int.* **2006**, *165*, 705–718. [CrossRef]
21. Khalil, M.A.; Hafez, M.A.; Santos, F.M.; Ramalho, E.C.; Mesbah, H.S.; El-Qady, G.M. An approach to estimate porosity and groundwater salinity by combined application of GPR and VES: A case study in the Nubian sandstone aquifer. *Near Surf. Geophys.* **2010**, *8*, 223–233. [CrossRef]
22. Alam, K.; Ahmad, N. Determination of aquifer geometry through geophysical methods: A case study from Quetta Valley, Pakistan. *Acta Geophys.* **2014**, *62*, 142–163. [CrossRef]
23. Farzamian, M.; Monteiro Santos, F.A.; Khalil, M.A. Estimation of unsaturated hydraulic parameters in sandstone using electrical resistivity tomography under a water injection test. *J. Appl. Geophys.* **2015**, *121*, 71–83. [CrossRef]
24. Binley, A.; Hubbard, S.S.; Huisman, J.A.; Revil, A.; Robinson, D.A.; Singha, K.; Slater, L.D. The emergence of hydrogeophysics for improved understanding of subsurface processes over multiple scales. *Water Resour. Res.* **2015**, *51*, 3837–3866. [CrossRef] [PubMed]
25. Gonçalves, R.; Farzamian, M.; Monteiro Santos, F.A.; Represas, P.; Mota Gomes, A.; Lobo de Pina, A.F.; Almeida, E.P. Application of time-domain electromagnetic method in investigating saltwater intrusion of Santiago Island (Cape Verde). *Pure Appl. Geophys.* **2017**, *174*, 4171–4182. [CrossRef]
26. Giustiniani, M.; Accaino, F.; Picotti, S.; Tinivella, U. Characterization of the shallow aquifers by high-resolution seismic data. *Geophys. Prospect.* **2008**, *56*, 655–666. [CrossRef]
27. Martorana, R.; Lombardo, L.; Messina, N.; Luzio, D. Integrated geophysical survey for 3D modelling of a coastal aquifer polluted by seawater. *Near Surf. Geophys.* **2014**, *12*, 45–59. [CrossRef]
28. Foti, S.; Hollender, F.; Garofalo, F.; Albarello, D.; Asten, M.; Bard, P.Y.; Comina, C.; Cornou, C.; Cox, B.; Giulio, G.D.; et al. Guidelines for the good practice of surface wave analysis: A product of the InterPACIFIC project. *Bull. Earthq. Eng.* **2018**, *16*, 2367–2420. [CrossRef]
29. Xia, J.; Miller, R.D.; Park, C.B. Estimation of near-surface shear-wave velocity by inversion of Rayleigh wave. *Geophysics* **1999**, *64*, 691–700. [CrossRef]
30. Xia, J.; Miller, R.D.; Park, C.B.; Hunter, J.A.; Harris, J.B.; Ivanov, J. Comparing shear-wave velocity profiles inverted from multichannel surface wave with borehole measurements. *Soil Dyn. Earthq. Eng.* **2002**, *22*, 181–190. [CrossRef]
31. Park, C.B.; Miller, R.D.; Xia, J. Multi-channel analysis of surface waves. *Geophysics* **1999**, *64*, 800–808. [CrossRef]
32. Park, C.B.; Miller, R.D.; Xia, J.; Ivanov, J. Multichannel analysis of surface waves (MASW)—Active and passive methods. *Lead Edge* **2007**, *26*, 60–64. [CrossRef]
33. Paz, C.; Alcalá, F.J.; Carvalho, J.M.; Ribeiro, L. Current uses of ground penetrating radar in groundwater-dependent ecosystems research. *Sci. Total Environ.* **2017**, *595*, 868–885. [CrossRef]
34. Bobeck, P. Henry Darcy in his own words. *Hydrogeol. J.* **2006**, *14*, 998–1004. [CrossRef]
35. Brown, G.O. Henry Darcy and the making of a law. *Water Resour. Res.* **2002**, *38*, 1106. [CrossRef]
36. Chen, D.; Chen, H.W. Using the Köppen classification to quantify climate variation and change: An example for 1901–2010. *Environ. Dev.* **2013**, *6*, 69–79. [CrossRef]
37. Herrera, S.; Cardoso, R.M.; Soares, P.M.M.; Espírito-Santo, F.; Viterbo, P.; Gutiérrez, J.M. Iberia01: A new gridded dataset of daily precipitation and temperatures over Iberia. *Earth Syst. Sci. Data* **2019**, *11*, 1947–1956. [CrossRef]
38. IGME. *Geological Map of Spain, Scale 1:50,000*; Sheet n° 1057 Adra. Geological Survey of Spain, Memory and Maps; IGME: Madrid, Spain, 1983; Available online: <http://info.igme.es/cartografiadigital/geologica/Magna50.aspx> (accessed on 11 January 2021).
39. Sanz de Galdeano, C. *La Zona Interna Bético-Rifeña. Antecedentes, Unidades Tectónicas, Correlaciones y Bosquejo de Reconstrucción Paleogeográfica*; University of Granada: Granada, Spain, 1997; pp. 1–316.
40. Alcalá, F.J.; Guerrero, F.; Martín-Martín, M.; Raffaelli, G.; Serrano, F. Geodynamic implications derived from Numidian-like distal turbidites deposited along the Internal-External Domain Boundary of the Betic Cordillera (S, Spain). *Terra Nova* **2013**, *25*, 119–129. [CrossRef]
41. Goy, J.L.; Zazo, C. Synthesis of the Quaternary in the Almería littoral neotectonic activity and its morphologic features, western Betics, Spain. *Tectonophysics* **1986**, *130*, 259–270. [CrossRef]
42. Pulido-Bosch, A.; Morales, G.; Benavente, J. Hidrogeología del delta del río Adra. *Estud. Geológicos* **1988**, *44*, 429–443. [CrossRef]
43. IGME. *Hydrogeological Map of Spain, Scale 1:200,000*; Sheet n° 84, Almería; Geological Survey of Spain, Memory and Maps; IGME: Madrid, Spain, 1988; Available online: <http://info.igme.es/cartografiadigital/tematica/Hidrogeologico200.aspx> (accessed on 11 January 2021).
44. IGME. *Hydrogeological Atlas of Andalusia. Geological Survey of Spain*; IGME: Madrid, Spain, 1998; Available online: https://aguas.igme.es/igme/publica/libros1_HR/libro110/lib110.htm (accessed on 11 January 2021).

45. INE. *Official Population Figures of Spanish Municipalities: Review of the Municipal Register—Population at 01 January 2019*; Spanish National Institute for Statistics: Madrid, Spain, 2019; Available online: <https://www.ine.es/jaxiT3/Datos.htm?t=2857#!tabs-tabla> (accessed on 29 December 2020).
46. JUNTA. *Hydrographic Demarcation of the Andalusian Mediterranean Basins—Appendix III: Uses and Demands*; Ministry of Agriculture, Fishery and Environment, Government of Andalusia: Sevilla, Spain, 2015; pp. 1–133.
47. CENTER. *Evaluation of the San Fernando Canal Irrigation Community. Municipal district of Adra (Almería)*; Ministry of Agriculture, Fishery and Feeding, Government of Spain: Madrid, Spain, 2007; pp. 1–161.
48. Alcalá, F.J.; Zapata, A.; Morillas-Arcos, M. Estructuras de detención/retención en la localidad de Adra (Almería). Posible alternativa al aprovechamiento de aguas pluviales. In *V Simposio Sobre el Agua en Andalucía*, 1st ed.; Pulido-Bosch, A., Pulido-Leboeuf, P.A., Vallejos-Izquierdo, A., Eds.; University of Almería: Almería, Spain, 2001; Volume 1, pp. 143–154.
49. ARWUA. *Groundwater Balance of the Adra River Alluvial Aquifer at Los Hurtados-Las Checas Place (Adra, Almería)*; Memory and Appendices; Adra River Water Users Association: Adra, Spain, 2007.
50. CSIC. *Scientific-Technical Advice to Study the Hydrogeological Ground Behavior on the Site and Neighbouring to the San Andrés III and San Andrés IV Buildings, Located at 12 and 14 Portón Street, in Adra Town (Almería)*; Memory and Appendices; Spanish National Research Council: Almería, Spain, 2010.
51. Benavente, J.; Castillo, A. Estudio Hidrogeoquímico de la cuenca del río Adra. *Estud. Geológicos* **1989**, *45*, 81–90. [[CrossRef](#)]
52. González-López, J. Water Resources Evaluation of the Adra River Valley Alluvial Aquifer, Almería Province. Bachelor's Thesis, Catholic University of Murcia, Murcia, Spain, 2015.
53. Martínez-Pagán, P.; Navarro, M.; Pérez-Cuevas, J.; Alcalá, F.J.; García-Jerez, A.; Vidal, F. Shear-wave velocity structure from MASW and SPAC methods. The case of Adra town, SE Spain. *Near Surf. Geophys.* **2018**, *16*, 356–371. [[CrossRef](#)]
54. Lunt, I.A.; Hubbard, S.S.; Rubin, Y. Soil moisture content estimation using ground penetrating radar reflection data. *J. Hydrol.* **2015**, *307*, 254–269. [[CrossRef](#)]
55. Annan, A.P. GPR—History, trends, and future developments. *Subsurf. Sens. Technol. Appl.* **2002**, *3*, 253–270. [[CrossRef](#)]
56. Beres, M.; Haeni, F.P. Application of ground-penetrating radar methods in hydrogeologic studies. *Ground Water* **1991**, *29*, 375–386. [[CrossRef](#)]
57. Cassidy, N.J. Electrical and magnetic properties of rocks, soils and fluids. In *Ground Penetrating Radar: Theory and Applications*, 1st ed.; Jol, H.M., Ed.; Elsevier: Amsterdam, The Netherlands, 2009; pp. 41–72.
58. Neal, A. Ground penetrating radar and its use in sedimentology: Principles, problems and progress. *Earth-Sci. Rev.* **2004**, *66*, 261–330. [[CrossRef](#)]
59. Bano, M.; Marquis, G.; Nivière, B.; Maurin, J.C.; Cushing, M. Investigating alluvial and tectonic features with ground-penetrating radar and analyzing diffractions patterns. *J. Appl. Geophys.* **2000**, *43*, 33–41. [[CrossRef](#)]
60. Paz, C.; Alcalá, F.J.; Ribeiro, L. Ground penetrating radar attenuation expressions in shallow groundwater research. *J. Environ. Eng. Geophys.* **2020**, *25*, 153–160. [[CrossRef](#)]
61. Van Dam, R.L.; Schlager, W. Identifying causes of ground-penetrating radar reflections using time-domain reflectometry and sedimentological analyses. *Sedimentology* **2000**, *47*, 435–449. [[CrossRef](#)]
62. Paz, M.C.; Alcalá, F.J.; Medeiros, A.; Martínez-Pagán, P.; Pérez-Cuevas, J.; Ribeiro, L. Integrated MASW and ERT imaging for geological definition of an unconfined alluvial aquifer sustaining a coastal groundwater-dependent ecosystem in southwest Portugal. *Appl. Sci.* **2020**, *10*, 5905. [[CrossRef](#)]
63. García-Jerez, A.; Navarro, M.; Alcalá, F.J.; Luzón, F.; Pérez-Ruiz, J.A.; Enomoto, T.; Vidal, F.; Ocaña, E. Shallow velocity structure using joint inversion of array and h/v spectral ratio of ambient noise: The case of Mula town (SE of Spain). *Soil Dyn. Earthq. Eng.* **2007**, *27*, 907–919. [[CrossRef](#)]
64. Mitchell, J.K.; Soga, K. *Fundamentals of Soil Behaviour*, 3rd ed.; Wiley: London, UK, 2005; pp. 1–592.
65. Zimmer, M.A.; Prasad, M.; Mavko, G.; Nur, A. Seismic velocities of unconsolidated sands: Part 1—Pressure trends from 0.1 to 20 MPa. *Geophysics* **2007**, *72*, E1–E13. [[CrossRef](#)]
66. McGann, C.R.; Bradley, B.A.; Cubrinovski, M. Investigation of shear wave velocity depth variability, site classification, and liquefaction vulnerability identification using a near-surface Vs model of Christchurch, New Zealand. *Soil Dyn. Earthq. Eng.* **2017**, *92*, 692–705. [[CrossRef](#)]
67. Navarro, M.; Vidal, F.; Enomoto, T.; Alcalá, F.; García-Jerez, A.; Sánchez, F.J.; Abeki, N. Analysis of the weightiness of site effects on reinforced concrete (RC) building seismic behavior. The Adra town example (SE Spain). *Earthq. Eng. Struct. Dyn.* **2007**, *36*, 1363–1383. [[CrossRef](#)]
68. Andreu, J.M.; Alcalá, F.J.; Vallejos, Á.; Pulido-Bosch, A. Recharge to aquifers in SE Spain: Different approaches and new challenges. *J. Arid Environ.* **2011**, *75*, 1262–1270. [[CrossRef](#)]
69. Martínez-Pagán, P.; Navarro, M.; Pérez-Cuevas, J.; Alcalá, F.J.; García-Jerez, A.; Sandoval-Castaño, S. Shear-wave velocity based seismic microzonation of Lorca city (SE Spain) from MASW analysis. *Near Surf. Geophys.* **2014**, *12*, 739–749. [[CrossRef](#)]
70. Lerner, D.N. Identifying and quantifying urban recharge: A review. *Hydrogeol. J.* **2002**, *10*, 143–152. [[CrossRef](#)]
71. Vázquez-Suñé, E.; Sánchez-Vila, X.; Carrera, J. Introductory review of specific factors influencing urban groundwater, an emerging branch of hydrogeology, with reference to Barcelona, Spain. *Hydrogeol. J.* **2004**, *13*, 522–533. [[CrossRef](#)]
72. Schirmer, M.; Leschik, S.; Musolf, A. Current research in urban hydrogeology—A review. *Adv. Water Resour.* **2013**, *51*, 280–291. [[CrossRef](#)]

73. Asebriy, L.; Cherkaoui, T.; El Amrani-El Hassani, I.; Franchi, R.; Guerrero, F.; Martín-Martín, M.; Guerrero-Patamà, C.; Raffaelli, G.; Robles-Marín, P.; Tejera de León, J.; et al. Deterioration processes on archaeological sites of Chellah and Oudayas (world cultural heritage, Rabat, Morocco): Restoration test and recommendations. *Ital. J. Geosci.* **2009**, *128*, 157–171.
74. Luberti, G.M.; Vergar, F.; Marin, R.; Pica, A.; Del Monte, M. Anthropogenic modifications to the drainage network of Rome (Italy): The case study of the Aqua Mariana. *Alp. Mediterr. Quat.* **2018**, *31*, 119–132.
75. Forno, M.G.; De Luca, D.; Bonasera, M.; Bucci, A.; Gianotti, F.; Lasagna, M.; Lucchesi, S.; Pelizza, S.; Piana, F.; Taddia, G. Synthesis on the Turin subsoil stratigraphy and hydrogeology (NW Italy). *Alp. Mediterr. Quat.* **2018**, *31*, 147–170.
76. Alcalá, F.J.; Cantón, Y.; Contreras, S.; Were, A.; Serrano-Ortiz, P.; Puigdefábregas, J.; Solé-Benet, A.; Custodio, E.; Domingo, F. Diffuse and concentrated recharge evaluation using physical and tracer techniques: Results from a semiarid carbonate massif aquifer in southeast Spain. *Environ. Earth Sci.* **2011**, *62*, 541–557. [[CrossRef](#)]
77. Pulido-Velazquez, D.; Romero, J.; Collados-Lara, A.J.; Alcalá, F.J.; Fernández-Chacón, F.; Baena-Ruiz, L. Using the turnover time index to identify potential strategic groundwater resources to manage droughts within continental Spain. *Water* **2020**, *12*, 3281. [[CrossRef](#)]